IEEE Access
Multidisciplinary | Rapid Review | Open Access Journal

Received August 30, 2020, accepted September 14, 2020, date of publication September 18, 2020,
date of current version September 30, 2020.

Digital Object Identifier 10.1109/ACCESS.2020.3024788

Cycle Slips Detection for Triple-Frequency Signals of BDS by Combining Carrier Phase and Doppler Measurements

ZENGKAI SHI, XURONG DONG, XIANGXIANG FAN, GANG ZHANG, AND ZHAOYONG QIAN
Department of Space Information, Space Engineering University, Beijing 101416, China
Corresponding author: Zengkai Shi (zkshi1213@sina.com)

This work was supported by the National Natural Science Foundation of China under Grant 41574010.

ABSTRACT A new model is presented to resolve cycle slips detection for triple-frequency observations of BeiDou navigation satellite system (BDS) in this article when pseudorange observations are missing or insufficiently accurate under harsh or special situations. Based on the first-order time-difference geometry-free (GF) pseudorange-phase combination model, the new cycle slips detection and correction method based on the triple-frequency carrier phase and Doppler observations is proposed. With analyses on the two common sampling intervals (30 s and 1 s), it can be concluded that the optimal combination coefficients of the proposed model relate to sampling intervals. Combinations [4, −2, −3], [−1, −5,6], and [−3,6, −2] are selected to detect and correct cycle slips for 30 s sampling interval, while combinations [0, −1,1], [1,0, −1], and [−3,2,2] are selected for 1 s sampling interval. The validity of the phase-Doppler combination model under the static condition and the steady ionosphere with 30 s sampling interval and 1 s sampling interval is verified by two static experiments. Results show that the phase-Doppler combination model can achieve the same performance as the pseudorange-phase combination model. All the small, insensitive, and large cycle slips added to the three types of BDS satellites which separately belong to Geostationary Earth Orbit (GEO), Inclined Geosynchronous Orbit (IGSO), and Medium Earth Orbit (MEO) are detected and corrected successfully by the proposed model.

INDEX TERMS Triple-frequency, BDS, cycle slips detection, geometry-free pseudorange-phase combination model, phase-Doppler combination model.

I. INTRODUCTION

"Positioning, Navigation, Timing" (PNT) is an important national strategy in countries such as America and China, while Global Navigation Satellite System (GNSS) plays a most crucial role in PNT [1]. Generally, GNSS has three types of measurements, which are carrier phase observation, pseudorange observation, and Doppler shift. Since the carrier phase observations have high precision, they are widely used in many precise positioning techniques. Meanwhile, the cycle slip is often inevitable. It is a discontinuity of an integer number of cycles in the carrier phase observations, and it generally results from signal interruption, low signal noise ratio (SNR) or breakdown of the receiver [2], [3]. If a cycle slip is ignored or cannot be correctly identified and corrected, it will affect carrier phase observations and lead to deviation in the ultimate positioning results. So the cycle slips detection and correction methods are essential.

Cycle slips detection and correction methods have been widely researched for several decades [4]. However, on the whole, based on the different types of observations used, the existing methods can be classified into two types. The first type is based on a single observation type (carrier phase observation) alone. Beutler and Davidson proposed polynomial fitting method in 1984, and Hofmann-Wellenhof *et al.* provided the high-order between-epoch phase differentiation in 2008. However, both methods can only detect large cycle slips and are insensitive to small cycle slips [5], [6]. Feng *et al.* put forward a modified geometry-free (GF) phase-only linear combination to quickly determine cycle slips for high-sampling-rate-multi-GNSS real-time kinematic positioning [7]. Cocard *et al.* presented the

The associate editor coordinating the review of this manuscript and approving it for publication was Seung-Hyun Kong.

GF combinations for the triple-frequency phase measurements [8]. Nevertheless, both methods are deeply affected by sampling interval and ionospheric activity. Therefore, combined with other observation types, cycle slips detection methods are further studied and improved by many researchers in the past decades.

At present, the second type is based on the combination of two observation types, which are mainly pseudorange/phase and phase/Doppler observations. Moreover, the former is the most studied over the world. By imposing position-based polynomial constraint, Li *et al.* proposed a new method for single-frequency GNSS cycle slip estimation, but it is only for single-frequency observations [9]. For dual-frequency observations, the most famous method is the TurboEdit algorithm which uses the Hatch-Melbourne-Wübbena (HMW) combination and GF combination [10]–[13]. However, owing to the ionospheric delay variation and the high pseudorange noise, it may gain incorrect cycle slips. Considering ionospheric activity, Cai *et al.* improved the TurboEdit algorithm based on the forward and backward moving window averaging algorithm and the first-order/second-order time-difference phase ionospheric residual (PIR/STPIR) algorithm [14]. However, the TurboEdit algorithm needs several minutes of continuous carrier phase data before and after a cycle slip. So the above two methods are not suitable to be used for real-time application [15]. Compared with dual-frequency signals, triple-frequency signals can provide more observation combinations, which will contribute to obtain better properties of models such as longer wavelengths, lower noises, and lower ionospheric errors. So cycle slips detection methods based on triple-frequency observations are also widely investigated [16]–[20]. Based on Least-squares Ambiguity Decorrelation Adjustment (LAMBDA), two GF phase combinations and one GF pseudorange-phase linear combination were used to detect cycle slips by Huang *et al.* [21]. But the method only applies to smooth ionospheric delay variations. Zhao *et al.* proposed another method based on the traditional extra-wide-lane HMW combination and modified HMW combinations [22]. And results showed that the proposed method could provide a 100% success rate in detecting cycle slips. Li *et al.* presented a geometry-based ionosphere-weighted approach to estimate integer cycle slips with taking full advantage of the mutual correlations between multi-frequencies, between satellites, and between systems [23]. And to solve ''blind detection spots'' problem, Yin *et al.* proposed a complementary symmetric GF (CSGF) method and a CSGF second-order differential model to detect cycle slips [24]. Besides, Kalman filter is also used to detect cycle slips. Li *et al.* put forward a novel method based on a Kalman-filter-based procedure with the undifferenced and uncombined precise point positioning (PPP) model [25]. Considering the impact of ionospheric delay, Chang *et al.* developed an adaptive Kalman filter based on variance component estimation to aid the cycle slips detection [26]. But Kalman filter may increase the time complexity and the space complexity of the algorithm.

However, another type based on the combination of carrier phase and Doppler observations is limited. Cannon *et al.* proposed a method that the phase measurement at the current epoch was predicted by the previous observations of carrier phase and Doppler at a high sampling rate [27]. Cederholm and Plausinaitis used expected Doppler shift to identify cycle slips [28]. Doppler cycle slips detection method was also studied by Dai, but limitation was the sampling interval and the degraded quality of Doppler observations [29]. Xu used an external instantaneous Doppler integration and fitted the Doppler data with a suitable order polynomial for cycle slips detection. But the order should be confirmed in advance [30]. Zhao *et al.* introduced a high-rate Doppler-aided cycle slips detection and repair (DACS-DR) method to detect and repair cycle in single-frequency low-cost GNSS receiver [31]. But all the above methods are based on single-frequency, and they are deeply affected by sampling intervals. They cannot detect some small or particular cycle slips as well. Unfortunately, studies on the triple-frequency phase and Doppler measurements are few.

In summary, most researches of cycle slips detection methods focus on carrier phase and pseudorange observations [32]. And their performance is better than that of the first type. So they are widely used to detect cycle slips under different situations. However, on the one hand, the most important precondition is that pseudorange observations at the corresponding epochs must exist. Unfortunately, some harsh or special situations where pseudorange observations are insufficient or poor exist in the practical work. Meanwhile, methods with only phase observations or methods based on single-frequency phase/Doppler observations cannot detect small or insensitive cycle slips, and they are easily influenced by the ionospheric activity. On the other hand, triple-frequency signals can provide more observation combinations that will help to obtain better properties of a model. Therefore, combinations of the triple-frequency phase observations and Doppler observations for cycle slips detection and correction are worth studying.

In this article, firstly, as a reference, the first-order time-difference GF pseudorange-phase combination model is introduced. Then a new cycle slips detection and correction model based on the triple-frequency phase and Doppler observations of BeiDou navigation satellite system (BDS) is proposed. In the subsequent section, the optimal combinations, the underlying mechanism, and advantages of the proposed model are discussed. At last, data from two static experiments are used to confirm the validity of the proposed model under 30 s and 1 s sampling intervals. Conclusions are followed.

II. CYCLE SLIPS DETECTION AND CORRECTION MODEL

A. BDS BASIC OBSERVATION MODEL

Generally, the undifferenced pseudorange, carrier phase, and Doppler observation equations can be expressed as [15], [30]:

$$P_i = \rho + q_i I + \varepsilon_{P_i} \tag{1}$$

$$\lambda_i\varphi_i = \rho - q_i I + \lambda_i N_i + \lambda_i \varepsilon_{\varphi_i} \tag{2}$$

$$D_i = -\frac{d(\rho - q_i I)}{\lambda_i dt} + \varepsilon_{D_i} \tag{3}$$

where the subscript $i (i = 1, 2, 3)$ refers to the three frequencies of BDS. P_i is the pseudorange measurement in units of meters. φ_i and D_i represent the carrier phase observation in units of cycles and the Doppler observation in units of Hz. The symbol ρ (in meters) is the geometric distance between satellite and receiver, which also includes the tropospheric error, the satellite and receiver clock error, and the receiver and satellite hardware delay. I (in meters) denotes the ionospheric delay at frequency f_1, and $q_i = f_1^2/f_i^2$ is the ionospheric scale factor (ISF) which represents the amplification factor of different frequencies. λ_i is the carrier wavelength (in meters), and N_i means the integer ambiguity. ε_{P_i}, ε_{φ_i}, and ε_{D_i} are pseudorange noise (in meters), carrier phase observations noise (in cycles), and Doppler observations noise (in Hz), respectively. Doppler shift increases as distance decreases. So D_i will be positive if the distance between the receiver and satellite decreases, and when the distance between the receiver and satellite increases, it will be negative. In addition, according to the actual values of Doppler observations in the observation file of BDS, the negative sign on the right of (3) is essential.

B. BDS LINEARLY COMBINED TRIPLE-FREQUENCY CARRIER PHASE AND PSEUDORANGE OBSERVATION

The geometry-based, linearly combined triple-frequency carrier phase observation equation is defined as [33]:

$$\begin{aligned}\lambda_{(i,j,k)}\varphi_{(i,j,k)} &= \frac{if_1\lambda_1\varphi_1 + jf_2\lambda_2\varphi_2 + kf_3\lambda_3\varphi_3}{if_1 + jf_2 + kf_3} \\ &= \rho - \beta_{(i,j,k)} I + \lambda_{(i,j,k)} N_{(i,j,k)} + \lambda_{(i,j,k)}\varepsilon_{\varphi(i,j,k)}\end{aligned} \tag{4}$$

where $\varepsilon_{\varphi_{(i,j,k)}} = i\varepsilon_{\varphi_1} + j\varepsilon_{\varphi_2} + k\varepsilon_{\varphi_3}$, and the combination coefficients i, j, k are integers. $\beta_{(i,j,k)}$ represents the ISF of the combined signals, and is derived as:

$$\beta_{(i,j,k)} = \frac{f_1^2(i/f_1 + j/f_2 + k/f_3)}{if_1 + jf_2 + kf_3} \tag{5}$$

The linearly combined wavelength and integer ambiguity are:

$$\lambda_{(i,j,k)} = \frac{c}{if_1 + jf_2 + kf_3} \tag{6}$$

$$N_{(i,j,k)} = iN_1 + jN_2 + kN_3 \tag{7}$$

Similarly, the geometry-based, linearly combined triple-frequency pseudorange observation equation is modelled as:

$$\begin{aligned}P_{(l,m,n)} &= lP_1 + mP_2 + nP_3 \\ &= \rho + \beta_{(l,m,n)} I + \varepsilon_{P_{(l,m,n)}}\end{aligned} \tag{8}$$

where $\varepsilon_{P_{(l,m,n)}} = l\varepsilon_{P_1} + m\varepsilon_{P_2} + n\varepsilon_{P_3}$.

$\beta_{(l,m,n)}$ is the ISF of $P_{(l,m,n)}$, and is derived as:

$$\beta_{(l,m,n)} = l + m\frac{f_1^2}{f_2^2} + n\frac{f_1^2}{f_3^2} \tag{9}$$

where the combination coefficients l, m, n are real numbers and should meet the equation $l + m + n = 1$.

C. PSEUDORANGE-PHASE COMBINATION MODEL

To derive the phase-Doppler combination equations, pseudorange-phase combination model should be introduced first. Whereas pseudorange-phase combinations are usually based on first-order time-difference as well as second-order time-difference, only the former is discussed in this article. And it also contributes to comprehend the phase-Doppler combination model.

According to (4) and (8), the GF pseudorange-phase combination can be expressed as:

$$\begin{aligned}&\varphi_{(i,j,k)} - \frac{P_{(l,m,n)}}{\lambda_{(i,j,k)}} \\ &\quad = -Q_{(i,j,k,l,m,n)} I + N_{(i,j,k)} + \varepsilon_{\varphi_{(i,j,k)}} - \frac{\varepsilon_{P_{(l,m,n)}}}{\lambda_{(i,j,k)}}\end{aligned} \tag{10}$$

where $Q_{(i,j,k,l,m,n)} = (\beta_{(l,m,n)} + \beta_{(i,j,k)})/\lambda_{(i,j,k)}$. From (10), it can be concluded that the GF pseudorange-phase combination can eliminate the geometric distance between satellite and receiver, the satellite and receiver clock error, the tropospheric delay, as well as the satellite and receiver hardware delay.

The GF pseudorange-phase combination based on the first-order time-difference can be derived as:

$$\begin{aligned}&\Delta\varphi_{(i,j,k)} - \frac{\Delta P_{(l,m,n)}}{\lambda_{(i,j,k)}} \\ &\quad = -Q_{(i,j,k,l,m,n)}\Delta I + \Delta N_{(i,j,k)} + \Delta\varepsilon_{\varphi_{(i,j,k)}} - \frac{\Delta\varepsilon_{P_{(l,m,n)}}}{\lambda_{(i,j,k)}}\end{aligned} \tag{11}$$

where Δ denotes the first-order time-difference between two consecutive epochs. $\Delta N_{(i,j,k)}$ refers to the cycle slip of the combination, ΔI denotes the first-order ionospheric delay variation. From the equation above, the inter-frequency biases and inter-observation-type biases can be neglected through the first-order time-difference algorithm, since the inter-frequency biases for pseduorange and phase of both receiver and satellite as well as the-observation-type biases can be deemed as constant over a short time span.

For two consecutive epochs $t0$ and $t1$, the estimated combined cycle slip $\Delta\tilde{N}_{(i,j,k)}$ on the triple-frequency phase combination $\varphi_{(i,j,k)}$ can be defined as:

$$\begin{aligned}\Delta\tilde{N}_{(i,j,k)} = \Delta\varphi_{(i,j,k)} - \frac{\Delta P_{(l,m,n)}}{\lambda_{(i,j,k)}} &= [\varphi_{(i,j,k)}(t1) \\ &\quad -\varphi_{(i,j,k)}(t0)] - [P_{(l,m,n)}(t1) \\ &\quad -P_{(l,m,n)}(t0)]/\lambda_{(i,j,k)}\end{aligned} \tag{12}$$

Assuming that the noise terms of the carrier phase observations on each frequency are independent in time and identical

in variance (i.e., $\sigma_\varphi = \sigma_{\varphi 1} = \sigma_{\varphi 2} = \sigma_{\varphi 3}$), and the noise terms of pseudorange observations are same (i.e., $\sigma_P = \sigma_{P1} = \sigma_{P2} = \sigma_{P3}$), the standard deviations (STDs) of the estimated first-order time-difference combined cycle slip $\Delta\tilde{N}_{(i,j,k)}$ can be calculated by:

$$\begin{aligned}\sigma_{\Delta N_{(i,j,k)}} &= \sqrt{\sigma^2_{\Delta\varphi_{(i,j,k)}} + \sigma^2_{\Delta P_{(l,m,n)}}/\lambda^2_{(i,j,k)}} \\ &= \sqrt{2(i^2+j^2+k^2)\sigma^2_\varphi + 2(l^2+m^2+n^2)\sigma^2_P/\lambda^2_{(i,j,k)}}\end{aligned} \tag{13}$$

If $\sigma_{\Delta N_{(i,j,k)}}$ is sufficiently small, a small bias in float cycle slip estimation can hardly affect the cycle slip fixing. Then with making a comparison between (11) and (12), it can be inferred that:

$$\begin{aligned}\delta_{\Delta N_{(i,j,k)}} &= \Delta N_{(i,j,k)} - \Delta\tilde{N}_{(i,j,k)} \\ &= Q_{(i,j,k,l,m,n)}\Delta I - \Delta\varepsilon_{\varphi_{(i,j,k)}} + \frac{\Delta\varepsilon_{P_{(l,m,n)}}}{\lambda_{(i,j,k)}}\end{aligned} \tag{14}$$

where $\delta_{\Delta N_{(i,j,k)}}$ refers to the value of $\Delta N_{(i,j,k)}$ minus $\Delta\tilde{N}_{(i,j,k)}$. And large combined wavelength can decrease the influence of pseudorange noise in (14).

Algorithm of the pseudorange-phase combination model based on first-order time-difference is widely used in many situations. However, on the one hand, the noise of pseudorange can reach 3 m or even more significant in some situations, especially under the harsh environment, which will significantly reduce the success ratio of cycle slips detection. On the other hand, the valid pseudorange data may be insufficient in some situations. So researches on Doppler cycle slips detection are indispensable. Combined with the pseudorange-phase combination model above, the phase-Doppler combination model is studied and illustrated as follow.

D. PHASE-DOPPLER COMBINATION MODEL

For the time from $t0$ to $t1$, the Doppler equation (3) can be integrated as:

$$\begin{aligned}K_i &= -\lambda_i \int_{t0}^{t1} D_i dt = \Delta(\rho - q_i I) + \tilde{\varepsilon}_{D_i} \\ \tilde{\varepsilon}_{D_i} &= -\lambda_i \int_{t0}^{t1} \varepsilon_{D_i} dt\end{aligned} \tag{15}$$

where $\Delta(\rho - q_i I)$ denotes the change of $\rho - q_i I$ between $t0$ and $t1$.

For (1), the differenced pseudorange between $t0$ and $t1$ can be expressed as:

$$\Delta P_i = \Delta(\rho + q_i I) + \Delta\varepsilon_{P_i} \tag{16}$$

Then from (15) and (16), it can be inferred that:

$$\Delta P_i = K_i + 2\Delta q_i I - \tilde{\varepsilon}_{D_i} + \Delta\varepsilon_{P_i} \tag{17}$$

Similarly, from (8) and (17), the combined time differenced pseudorange observation can be also modelled as:

$$\begin{aligned}&\Delta P_{(l,m,n)} \\ &= l\Delta P_1 + m\Delta P_2 + n\Delta P_3 = (lK_1 + mK_2 + nK_3) \\ &\quad +2(l\Delta q_1 I + m\Delta q_2 I + n\Delta q_3 I) - (l\tilde{\varepsilon}_{D_1} + m\tilde{\varepsilon}_{D_2} + n\tilde{\varepsilon}_{D_3}) \\ &\quad +(l\Delta\varepsilon_{P_1} + m\Delta\varepsilon_{P_2} + n\Delta\varepsilon_{P_3})\end{aligned} \tag{18}$$

With (18) substituted to (11), it can be inferred that:

$$\begin{aligned}\Delta\varphi_{(i,j,k)} - \frac{K_{(l,m,n)}}{\lambda_{(i,j,k)}} &= W_{(i,j,k,l,m,n)}\Delta I + \Delta N_{(i,j,k)} \\ &\quad +\Delta\varepsilon_{\varphi_{(i,j,k)}} + \frac{\varepsilon_{D_{(l,m,n)}}}{\lambda_{(i,j,k)}}\end{aligned} \tag{19}$$

with

$$\begin{aligned}W_{(i,j,k,l,m,n)} &= (\beta_{(l,m,n)} - \beta_{(i,j,k)})/\lambda_{(i,j,k)} \\ K_{(l,m,n)} &= lK_1 + mK_2 + nK_3 \\ \varepsilon_{D_{(l,m,n)}} &= l\tilde{\varepsilon}_{D_1} + m\tilde{\varepsilon}_{D_2} + n\tilde{\varepsilon}_{D_3}\end{aligned} \tag{20}$$

Since the time interval $\Delta t = t1 - t0$ is sufficiently small, (15) can be expressed as [25]:

$$K_i = -\lambda_i \int_{t0}^{t1} D_i dt = -\lambda_i \frac{D_i^{t0} + D_i^{t1}}{2}\Delta t \tag{21}$$

Thus, it can be inferred that:

$$\begin{aligned}K_{(l,m,n)} = -\frac{1}{2}\Delta t(&l\lambda_1 D_1^{t0} + m\lambda_2 D_2^{t0} + n\lambda_3 D_3^{t0} \\ &+ l\lambda_1 D_1^{t1} + m\lambda_2 D_2^{t1} + n\lambda_3 D_3^{t1})\end{aligned} \tag{22}$$

Similarly, like (12), and with (22) substituted to (19), for the two consecutive epochs $t0$ and $t1$, the estimated combined cycle slip $\Delta\tilde{N}_{(i,j,k)}$ on the triple-frequency phase combination $\varphi_{(i,j,k)}$ can be defined as:

$$\begin{aligned}\Delta\tilde{N}_{(i,j,k)} = \Delta\varphi_{(i,j,k)} - \frac{K_{(l.m.n)}}{\lambda_{(i,j,k)}} &= [\varphi_{(i,j,k)}(t1) - \varphi_{(i,j,k)}(t0)] \\ &\quad +\frac{\Delta t}{2\lambda_{(i,j,k)}}(l\lambda_1 D_1^{t0} + m\lambda_2 D_2^{t0} + n\lambda_3 D_3^{t0} + l\lambda_1 D_1^{t1} \\ &\quad +m\lambda_2 D_2^{t1} + n\lambda_3 D_3^{t1})\end{aligned} \tag{23}$$

Assuming that the noise terms of the Doppler observations on each frequency are independent in time and are identical in variance (i.e., $\sigma_D = \sigma_{D1} = \sigma_{D2} = \sigma_{D3}$), the STDs of the estimated combined cycle slip $\Delta\tilde{N}_{(i,j,k)}$ is expressed as (24), as shown at the bottom of the next page:

Likewise, if $\sigma_{\Delta N_{(i,j,k)}}$ is sufficiently small, the correct cycle slip fixing can hardly be affected by a small bias in float cycle slip estimation. This article also defines

$$|\Delta\tilde{N}_{(i,j,k)}| \geq \kappa\sigma_{\Delta N_{(i,j,k)}} \tag{25}$$

to justify the occurrence of the cycle slip. From (23) and (24), it is the between-epoch difference of carrier phases rather than carrier phases themselves that are directly used to detect cycle

slips. And to be more specific, the between-epoch difference when a cycle slip occurs will make the corresponding noise satisfy (25) [26].

Then it can be derived from (19) and (23) that:

$$\delta_{\Delta N_{(i,j,k)}} = \Delta N_{(i,j,k)} - \Delta\tilde{N}_{(i,j,k)} = -W_{(i,j,k,l,m,n)}\Delta I - \Delta\varepsilon_{\varphi_{(i,j,k)}} - \frac{\Delta\tilde{\varepsilon}_{D_{(l,m,n)}}}{\lambda_{(i,j,k)}} \quad (26)$$

where $\delta_{\Delta N_{(i,j,k)}}$ refers to the value of $\Delta N_{(i,j,k)}$ minus $\Delta\tilde{N}_{(i,j,k)}$ like (14). And large combined wavelength can decrease the influence of Doppler noise as well.

Like pseudorange-phase combination model, the success rate can also be expressed as [34]:

$$P = 2\phi(0.5\sigma^{-1}_{\Delta N_{(i,j,k)}}) - 1$$
$$\phi(x) = \int_{-\infty}^{x} \frac{1}{2\pi}\exp\left(-\frac{1}{2}z^2\right)dz \quad (27)$$

E. CYCLE SLIPS CORRECTION

Once the cycle slips of three combinations are correctly detected, the integer triple-frequency cycle slips $\Delta\bar{N}_1$, $\Delta\bar{N}_2$, and $\Delta\bar{N}_3$ are finally determined by:

$$\begin{bmatrix}\Delta\bar{N}_1\\ \Delta\bar{N}_2\\ \Delta\bar{N}_3\end{bmatrix} = \mathrm{A}^{-1}\begin{bmatrix}\Delta\bar{N}_{(i_1,j_1,k_1)}\\ \Delta\bar{N}_{(i_2,j_2,k_2)}\\ \Delta\bar{N}_{(i_3,j_3,k_3)}\end{bmatrix} = \begin{bmatrix}i_1 & j_1 & k_1\\ i_2 & j_2 & k_2\\ i_3 & j_3 & k_3\end{bmatrix}^{-1}\begin{bmatrix}\Delta\bar{N}_{(i_1,j_1,k_1)}\\ \Delta\bar{N}_{(i_2,j_2,k_2)}\\ \Delta\bar{N}_{(i_3,j_3,k_3)}\end{bmatrix} \quad (28)$$

where $\Delta\bar{N}_{(i_1,j_1,k_1)}$, $\Delta\bar{N}_{(i_2,j_2,k_2)}$, and $\Delta\bar{N}_{(i_3,j_3,k_3)}$ are also integers. And they can be obtained by rounding the estimated combined cycle slip $\Delta\tilde{N}_{(i,j,k)}$. A-matrix must be a non-singular matrix. Then after the three original carrier phase observations are corrected by subtracting the $\Delta\bar{N}_1$, $\Delta\bar{N}_2$, and $\Delta\bar{N}_3$, the new value of $\Delta\tilde{N}_{(i,j,k)}$ will be recalculated by (23) and should be smaller than $\kappa\sigma_{\Delta N_{(i,j,k)}}$.

III. ANALYSIS ON THE PHASE-DOPPLER COMBINA-TION MODEL

A. THE COMBINATION COEFFICIENTS

In this section, the six combination coefficients are discussed. In the above equations, the combination coefficients l, m, n are real numbers with a sum of 1. In addition, to reduce the impact of noises and the first-order ionospheric delay variations, the optimal phase-Doppler combinations based on first-order time-difference should comply with the following conditions (29)–(31), as shown at the bottom of the next page:

The frequency values of three carrier signals of BDS used in this article are listed in Table 1. Firstly, l, m, and n are considered. To make (30) small enough, $l^2\lambda_1^2 + m^2\lambda_2^2 + n^2\lambda_3^2$ should be reduced as much as possible. Based on the Arithmetic-Geometric mean inequality, it can be derived that $(l^2\lambda_1^2 + m^2\lambda_2^2 + n^2\lambda_3^2)/3 \geq \sqrt[3]{(lmn\lambda_1\lambda_2\lambda_3)^2}$. And only when $l^2\lambda_1^2 = m^2\lambda_2^2 = n^2\lambda_3^2$, $l^2\lambda_1^2 + m^2\lambda_2^2 + n^2\lambda_3^2$ can reach the minimum value. Compared with the pseudorange-phase combination model below, l, m, and n are all taken as positive values [21]. Thus, combined with (29), $l = 0.3867$, $m = 0.2990$, and $n = 0.3142$ are obtained to minimize (30) in this article.

TABLE 1. Carrier signals, frequencies, and wavelengths in BDS.

Carrier	f (MHz)	λ (m)
B1I	1561.098	0.192
B2I	1207.14	0.248
B3I	1268.52	0.236

Then optimal i, j, and k are selected from -10 to 10 in this section. However, (30) shows that the value of the time interval between two epochs will also influence $\sigma_{\Delta N_{(i,j,k)}}$. So two common time intervals ($\Delta t = 1$ s and 30 s) are studied in this article. Tables II-III show the optimal ten combinations of the phase-Doppler combination model within the range (−10, −10, −10) to (10,10,10) when $\sigma_\varphi = 0.01$ cycles and $\sigma_D = 0.3$ Hz [21], [28]. From the two tables, it can be concluded that the optimal combinations of phase-Doppler combination model will be greatly influenced by time intervals. The first three combinations under $\Delta t = 30$ s are [4, −2, −3], [−1, −5,6], and [−3,6, −2], while they are [0, −1,1], [1,0, −1], and [1, −1,0] under $\Delta t = 1$ s. In addition, when the time interval is smaller, $\sigma_{\Delta N_{(i,j,k)}}$ can also be smaller in (30). Owing to (25) and the cycle slip correction method in this article, the $\sigma_{\Delta N_{(i,j,k)}}$ should not be too large. That is to say, the STD of Doppler noise should not be too large. Otherwise, $4\sigma_{\Delta N_{(i,j,k)}}$ will exceed 0.5 cycles, and rounding the estimated combined cycle slip may not bring a reliable result. At this time, large combined wavelength and compensating for the large Doppler noise are needed. And rounding operation may be substituted by LAMBDA algorithm or modified LAMBDA algorithm, which should be further studied [3], [21]. On that account, Tables II-III also indicate that numbers of potential combinations under 30 s sampling interval are less than those under 1 s sampling interval in this article. And smaller STD of Doppler noise can also have more potential combinations.

Table 4 shows the optimal ten combinations of the pseudorange-phase combination model. The empirical value of σ_P and σ_φ are 0.3 m and 0.01 cycles. But the values of l, m, and n are different from the phase-Doppler combination model, and they are all equal to 1/3 [21]. From Tables II-IV, there exist obvious differences among the optimal combinations of the proposed model and the pseudorange-phase combination model.

$$\sigma_{\Delta N_{(i,j,k)}} = \sqrt{\sigma^2_{\Delta\varphi_{(i,j,k)}} + \sigma_K^2/\lambda^2_{(i,j,k)}} = \sqrt{2(i^2+j^2+k^2)\sigma_\varphi^2 + (l^2\lambda_1^2 + m^2\lambda_2^2 + n^2\lambda_3^2)\Delta t^2\sigma_D^2/(2\lambda^2_{(i,j,k)})} \quad (24)$$

TABLE 2. The optimal ten combinations which have small $\sigma_{\Delta N_{(i,j,k)}}$ of the phase-Doppler combination model under $\Delta t = 30$ s.

i	j	k	$\lambda_{(i,j,k)}$ (m)	$W_{(i,j,k,l,m,n)}$ (m^{-1})	$\sigma_{\Delta N_{(i,j,k)}}$ (cycles)
4	-2	-3	12.211	-11.976	0.101
-1	-5	6	20.932	-0.493	0.118
-3	6	-2	13.321	11.864	0.117
-4	1	4	8.140	11.371	0.129
7	-8	-1	146.526	-23.840	0.151
5	3	-9	29.305	-11.482	0.154
3	-7	3	7.712	-12.469	0.157
1	4	-5	6.371	-0.112	0.158
-8	3	7	24.421	23.347	0.160
0	-1	1	4.884	-0.605	0.169

TABLE 3. The optimal ten combinations which have small $\sigma_{\Delta N_{(i,j,k)}}$ of the phase-Doppler combination model under $\Delta t = 1$ s.

i	j	k	$\lambda_{(i,j,k)}$ (m)	$W_{(i,j,k,l,m,n)}$ (m^{-1})	$\sigma_{\Delta N_{(i,j,k)}}$ (cycles)
0	-1	1	4.884	-0.605	0.021
1	0	-1	1.025	-2.531	0.033
1	-1	0	0.847	-3.136	0.038
1	1	-2	1.297	-1.926	0.041
0	-2	2	2.442	-1.210	0.042
1	-2	1	0.722	-3.741	0.051
1	2	-3	1.765	-1.321	0.055
0	-3	3	1.628	-1.815	0.062
-3	2	2	1.119	9.445	0.063
-3	3	1	1.451	10.050	0.064

Generally, all the combinations can be clarified from three layers: the combined wavelength, the ISF ($W_{(i,j,k,l,m,n)}$), and the observation noise. From (30) and (31), it can be concluded that large combined wavelength will contribute to decreasing the influence of observation noise, while small ISF will help to reduce the bias resulting from the ionospheric activity. Moreover, although the combined noise of linearly combined triple-frequency observations will indeed larger than that of single-frequency observations, small combined observation noise is expected to increase the success rate of cycle slips detection in (27). But from Tables II-III, it is not easy to obtain three linear independent combinations whose ISFs and observation noises are all very small. So it is essential to select different combinations based on the actual situation. If the ionospheric activity is low, combinations with small combined noise can be chiefly considered to obtain a high success rate. If the ionospheric activity is high, combinations with small ISF should be chiefly considered, or ionospheric compensation is needed.

In the end, to test the effectiveness and availability of the phase-Doppler combination model under low ionospheric activity, small combined noise is considered first in this

TABLE 4. The optimal ten combinations which have small $\sigma_{\Delta N_{(i,j,k)}}$ of the pseudorange-phase combination model.

i	j	k	$\lambda_{(i,j,k)}$ (m)	$Q_{(i,j,k,l,m,n)}$ (m^{-1})	$\sigma_{\Delta N_{(i,j,k)}}$ (cycles)
0	-1	1	4.884	-0.040	0.041
4	-2	-3	12.211	-11.750	0.077
0	-2	2	2.442	-0.080	0.081
-4	1	4	8.140	11.710	0.084
4	-3	-2	3.489	-11.790	0.091
1	3	-4	2.765	0.281	0.096
1	4	-5	6.371	0.321	0.096
-3	5	-1	3.574	12.031	0.097
-3	6	-2	13.321	12.071	0.100
-1	-5	6	20.932	-0.362	0.112

TABLE 5. Optimal [*i,j,k*] and the success rate (*P*) of the phase-Doppler combination model for BDS cycle slips detection and correction under $\Delta t = 30$ s.

[*i,j,k*] Combinations	*P*
[4,-2,-3][-1,-5,6][-3,6,-2]	~100%
[4,-2,-3][-1,-5,6][7,-8,-1]	99.90%
[-3,6,-2][1,4,-5][0,1,-1]	99.53%
[-1,-5,6][5,3,-9][1,4,-5]	99.73%

article. Table 5 shows several optimal $[i,j,k]$ and the corresponding success rate of the phase-Doppler combination model for BDS cycle slips detection and correction, while $W_{(i,j,k,l,m,n)}$ is also considered and $\Delta t = 30$ s. Since the three combinations should be linearly independent. It can be seen that the optimal combinations for BDS are [4, −2, −3], [−1, −5,6], and [−3,6, −2]. And $W_{(i,j,k,l,m,n)}$ of [−1, −5,6] is -0.493 m^{-1}, which is relatively small. The success rate can reach almost 100%. But when the sampling interval is 1 s, the optimal combinations are [0, −1,1], [1,0, −1], and [−3,2,2]. The success rate also reaches almost 100%.

In addition, to ensure whether the ionosphere is steady or not, ΔI can be computed by using two of undifferenced triple-frequency phase observations [35]:

$$\Delta I = \frac{\Delta\varphi_1\lambda_1 - \Delta\varphi_3\lambda_3}{f_1^2/f_3^2 - 1} \tag{32}$$

whereas different orbit types have different velocities and ionosphere variations for BDS, it will be preferentially considered with the test data as well.

B. UNDERLYING MECHANISM AND ADVANTAGES

The underlying mechanism and advantages of the phase-Doppler combination model are presented as follow.

Doppler is an instantaneous measurement. And time differenced carrier phase observations between two consecutive epochs can be viewed as an integral of Doppler. Counting

$$l + m + n = 1 \tag{29}$$

$$\min : \sigma_{\Delta N_{(i,j,k)}} = \sqrt{2(i^2 + j^2 + k^2)\sigma_\varphi^2 + (l^2\lambda_1^2 + m^2\lambda_2^2 + n^2\lambda_3^2)\Delta t^2\sigma_D^2/(2\lambda_{(i,j,k)}^2)} \tag{30}$$

$$\min : -W_{(i,j,k,l,m,n)}\Delta I \tag{31}$$

TABLE 6. Two static cases.

Case	Latitude	Longitude	Sampling Interval (s)	Date	Location
case-1	40.33 °N	116.67 °E	30	July 29, 2019	China
case-2	40.31 °N	116.63 °E	1	July 14, 2018	China

cycles is an ingredient of the integration. Cycle slip is an error in the counting, and will only occur in the integration. In other words, only carrier phase measurement will be affected by the cycle slip, and it will not affect instantaneous Doppler measurements. So Doppler can be used to aid to detect cycle slips.

Although Doppler is usually used to measure the speed at present, the phase-Doppler combination model may provide a new application for triple-frequency Doppler measurements. And it can also be used for real-time application. In addition, there often exist missing data in the observation file. So the phase-Doppler combination model can be used to detect cycle slips when pseudorange observations are missing or insufficiently accurate. Moreover, it will also enrich the current cycle slips detection methods and may provide more detection combinations with other methods. For example, combined with GF and GIF methods, one combination of the phase-Doppler combination model may be used as the last detection combination.

IV. NUMERICAL RESULTS AND ANALYSES

Two static cases are used to verify the validity of the phase-Doppler combination model, which are marked as case-1 and case-2, respectively. Combined with the above section, two common sampling intervals (30 s and 1 s) are studied in this article. Table 6 lists the information of the two cases. The triple-frequency BDS observations of case-1 and case-2 were obtained from experiments in Huairou, Beijing, China on different dates. The observations of case-1 were collected with 30 s sampling interval from Global Positioning System (GPS) time 00:00:00 to 23:59:30 on 29 July 2019, while data of case-2 were on 14 July 2018 with 1 s sampling interval. Fig. 1 shows the situation of the experiment of case-1, which is also similar to case-2. And time reference used in this article is GPS time.

Moreover, owing to the different visible time of the same satellite in a different date, and to better verify the validity of the phase-Doppler combination model, BDS C05, C06, C08, C14, C25, and C26 that separately belong to Geostationary Earth Orbit (GEO), Inclined Geosynchronous Orbit (IGSO), and Medium Earth Orbit (MEO) are selected.

A. ANALYSIS ON IONOSPHERIC ACTIVITY

In this section, to judge whether ionosphere is steady or not, ionospheric activity is analyzed from two aspects. Firstly, the levels of ionospheric disturbances are analyzed with Kp index, which is a mean value of the geomagnetic disturbance

FIGURE 1. The situation of the case-1.

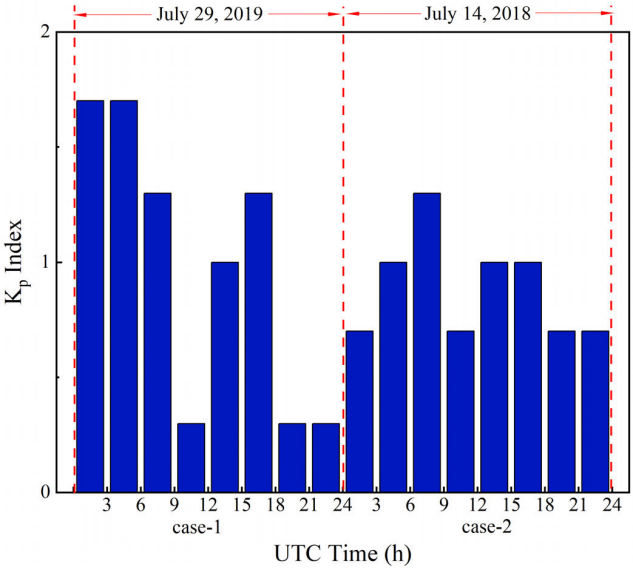

FIGURE 2. Kp index of the two cases.

levels denoting the severity of the global magnetic disturbances in near-earth space. Fig. 2 shows the Kp index released by the German Research Center for Geosciences (GFZ) on the above two dates. It is worth mentioning that although Kp index is given under UTC time, the gap of GPS time and UTC time is small and will not affect the conclusions. From Fig. 2, it can be seen that all the values of Kp index are smaller than 2. The average values of Kp index on the two dates are 1.00 and 0.875, respectively. So it can come to a conclusion that the ionosphere is steady and the ionospheric activity is low on the whole day.

However, since the Kp index is a global index, it may not reveal the local ionospheric variations accurately. So the ionospheric delay variation should also be further computed by (32). Owing to the different visible time of satellites, data insufficiency, and elevation angle, sometimes two satellites belonging to the same orbit are selected for the purpose that the time span of data can include a non-midday period as well

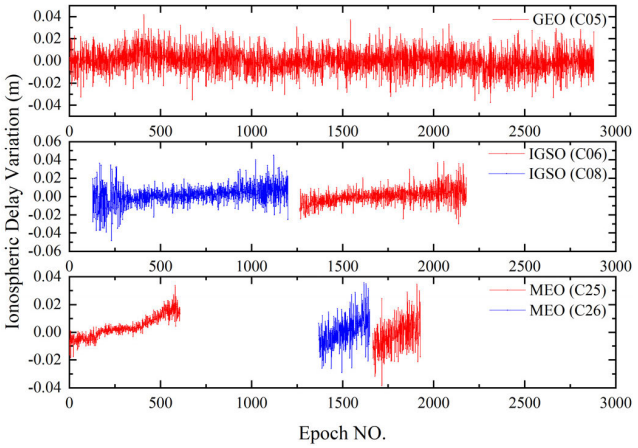

FIGURE 3. Between-epoch first order ionospheric delay variations (ΔI) for case-1.

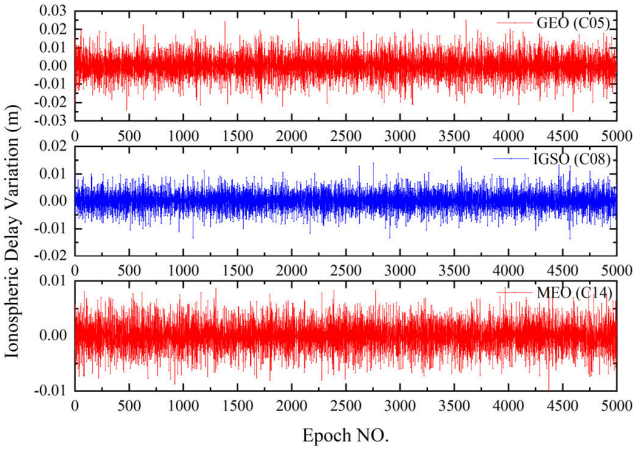

FIGURE 4. Between-epoch first order ionospheric delay variations (ΔI) for case-2.

as midday period. The midday is about GPS time 4:00 a.m. in Beijing.

Figs. 3-4 show the between-epoch first-order ionospheric delay variations (ΔI) for different satellites computed by (32). For simplicity, GPS time 00:00:00 is marked as epoch No. 1 in case-1. However, for case-2, owing to too many data, only about 5000 data that vary most are shown in Fig. 4. Since there exist many epochs when some data miss and have low elevation angles (the default cutting-off angle: 15°), the curves of IGSO and MEO are discontinuous in Fig. 3 [21].

From Fig. 3, it can be seen that almost all the ΔI data are smaller than 0.04 m with 30 s sampling interval. Most data are even smaller than 0.02 m, and the change rates are smaller than 0.067 cm/s. From Fig. 4, almost all the ΔI data of GEO are smaller than 0.02 m and the change rates are also smaller than 2 cm/s, while the ΔI data of IGSO and MEO are even smaller than 0.01 m. ΔI is also influenced by the sampling interval, and small interval relatively brings small ΔI. From the two figures, it can also be concluded that the ionosphere is steady and the ionospheric activity is low.

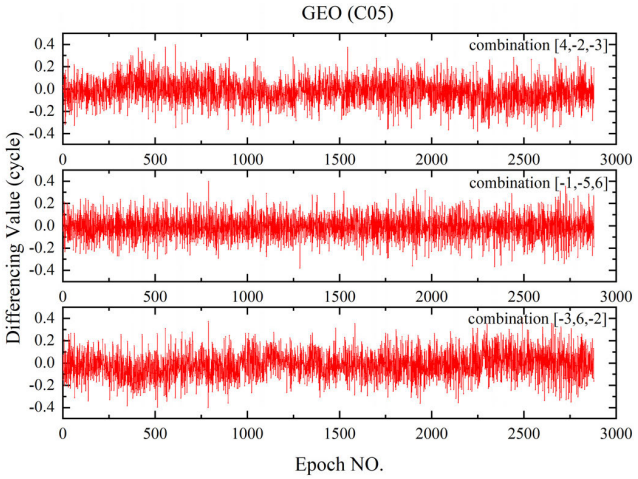

FIGURE 5. Differencing values ($\Delta\tilde{N}_{(i,j,k)}$) of the cycle slips detection combinations on GEO for case-1, when no cycle slip occurs.

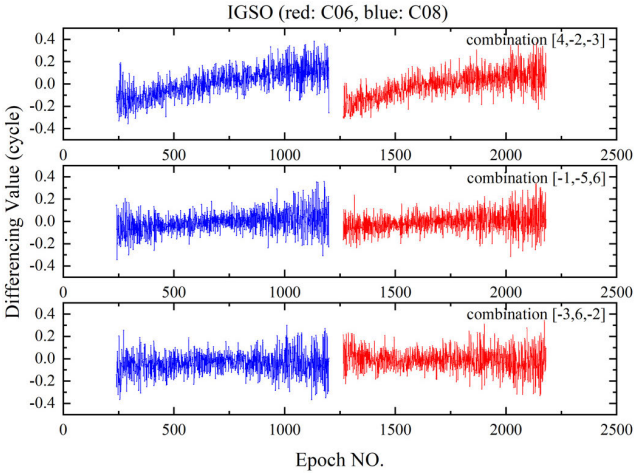

FIGURE 6. Differencing values ($\Delta\tilde{N}_{(i,j,k)}$) of the cycle slips detection combinations on IGSO for case-1, when no cycle slip occurs.

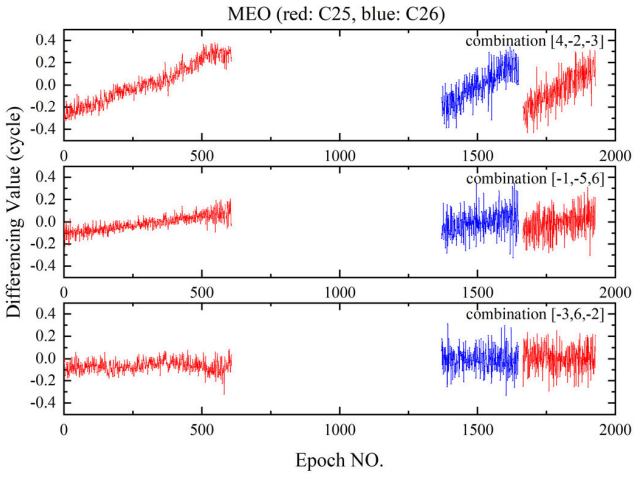

FIGURE 7. Differencing values ($\Delta\tilde{N}_{(i,j,k)}$) of the cycle slips detection combinations on MEO for case-1, when no cycle slip occurs.

Owing to steady ionosphere and low ionospheric activity, combinations with small combined noise are selected to detect and correct cycle slips. The linearly independent combinations [4, −2, −3], [−1, −5,6], and [−3,6, −2] are selected for case-1, while combinations [0, −1,1], [1,0, −1], and [−3,2,2] are selected for case-2. And threshold coefficient (κ) of cycle slips detection is set to 4 in (25).

B. CYCLE SLIPS DETECTION AND CORRECTION WITH CASE-1

According to the above section, linearly independent combinations [4, −2, −3], [−1, −5,6], and [−3,6, −2] are selected in case-1. Figs. 5-7 show the differencing values ($\Delta\tilde{N}_{(i,j,k)}$) of the cycle slips detection combinations on GEO, IGSO, and MEO when no cycle slip occurs. Combined with Table 2, all $\Delta\tilde{N}_{(i,j,k)}$ are smaller than $4\sigma_{\Delta N_{(i,j,k)}}$ and (25) is satisfied.

In the beginning, all the cycle slips that will be added to the phase data should be clarified. They can be divided into three types which are the small cycle slip (S), the insensitive cycle slip (I), and the large cycle slip (L), respectively. Moreover, the insensitive cycle slip can also be divided into two types. The first type that will be marked as I1 represents cycle slips which are only insensitive to one combination. For instance, the cycle slip (2,1,2) is only insensitive to combination [4, −2, −3], while it is sensitive to combination [−1, −5,6] and combination [−3,6, −2]. The second type that will be marked as I2 represents cycle slips which are simultaneously insensitive to two combinations. For instance, the cycle slip (27,21,22) is simultaneously insensitive to combination [4, −2, −3] and combination [−1, −5,6].

Then as done in Pu and Xiong [15], the above four different types of cycle slips are added to the phase data, which are (0,1,0) (S) and (1,1,0) (S), (2,1,2) (I1) and (2,2,2) (I1), (27,21,22) (I2) and (22,17,18) (I2), (1,3,3) (L) and (3,3,4) (L). The results of the cycle slips detection and correction by the phase-Doppler combination model are shown in Figs. 8-10 and listed in Table 7. Figs. 8-10 show that after the cycle slips are added on some epochs, obvious changes occur consistently. And A-matrix in (28) is

$$\mathrm{A} = \begin{bmatrix} 4 & -2 & -3 \\ -1 & -5 & 6 \\ -3 & 6 & -2 \end{bmatrix} \tag{33}$$

Combined with Table 7, it can be concluded that the most cycle slips added can be directly detected by the three linear independent combinations [4, −2, −3], [−1, −5,6], and [−3,6,−2]. And they can even detect and correct cycle slips as small as 1 cycle. For example, when the cycle slips (0,1,0), (1,1,0), (1,3,3), and (3,3,4) occur, all the differencing values of the three combinations have exceeded the cycle slips detection threshold in (25), while $\kappa = 4$ and $\sigma_{\Delta N_{(i,j,k)}}$ of the three combinations are 0.101, 0.118, and 0.117. However, for the insensitive cycle slips, there will exist one or two differencing values that do not exceed the cycle slip threshold. For example, the differencing value of combination [4, −2, −3] for the cycle slip (2,1,2) is 0.056, which do not satisfy (25).

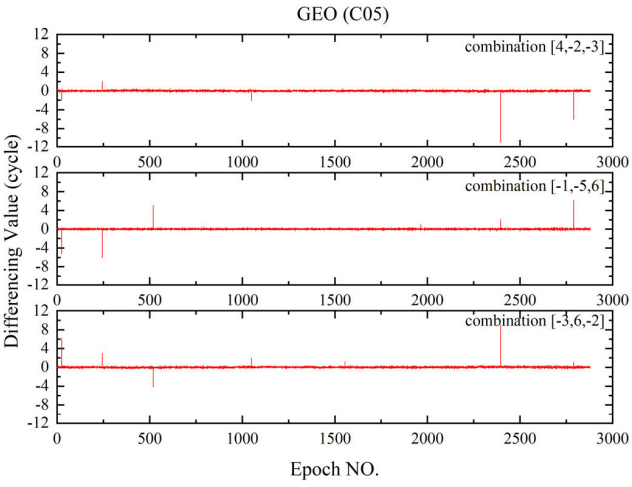

FIGURE 8. Differencing values ($\Delta\tilde{N}_{(i,j,k)}$) of the cycle slips detection combinations of the phase-Doppler combination model on GEO for case-1, when the four types of cycle slips are added.

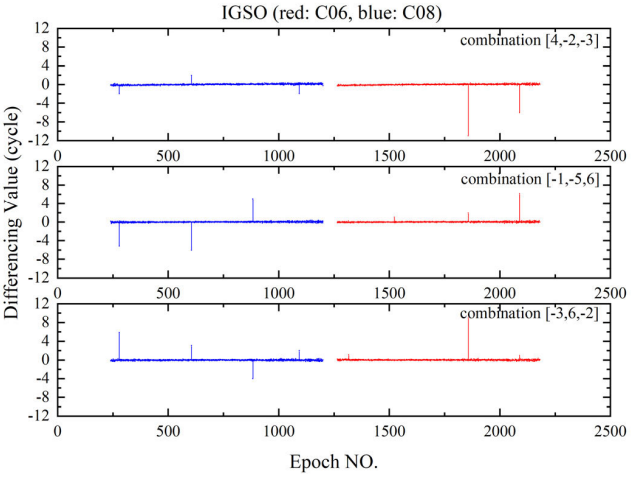

FIGURE 9. Differencing values ($\Delta\tilde{N}_{(i,j,k)}$) of the cycle slips detection combinations of the phase-Doppler combination model on IGSO for case-1, when the four types of cycle slips are added.

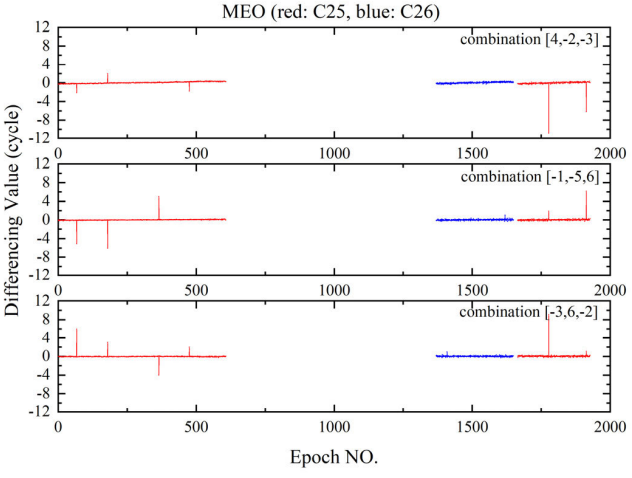

FIGURE 10. Differencing values ($\Delta\tilde{N}_{(i,j,k)}$) of the cycle slips detection combinations of the phase-Doppler combination model on MEO for case-1, when the four types of cycle slips are added.

TABLE 7. The detection performance of the phase-Doppler combination model when the four types of cycle slips are added to the three types of orbits for the three cases (∗: value that do not exceed the cycle slips detection threshold. The detection combinations are [4, −2, −3], [−1, −5,6], and [−3,6, −2] for case-1, while they are [0, −1,1], [1,0, −1], and [−3,2,2] for case-2).

Case	Orbit Type	Epoch NO.	Simulated Cycle Slip	Cycle Slip Type	$\Delta\tilde{N}_{(4,-2,-3)}$ or $\Delta\tilde{N}_{(0,-1,1)}$	$\Delta\tilde{N}_{(-1,-5,6)}$ or $\Delta\tilde{N}_{(1,0,-1)}$	$\Delta\tilde{N}_{(-3,6,-2)}$ or $\Delta\tilde{N}_{(-3,2,2)}$	$\Delta\bar{N}_{(4,-2,-3)}$ or $\Delta\bar{N}_{(0,-1,1)}$	$\Delta\bar{N}_{(-1,-5,6)}$ or $\Delta\bar{N}_{(1,0,-1)}$	$\Delta\bar{N}_{(-3,6,-2)}$ or $\Delta\bar{N}_{(-3,2,2)}$	Computed Integer Cycle Slip
case-1	GEO	25	[0,1,0]	S	-2.013	-5.137	6.094	-2	-5	6	[0,1,0]
		245	[1,1,0]	S	1.966	-5.979	2.885	2	-6	3	[1,1,0]
		519	[2,1,2]	I1	0.056*	4.955	-4.048	0	5	-4	[2,1,2]
		1051	[2,2,2]	I1	-2.049	-0.146*	1.877	-2	0	2	[2,2,2]
		1555	[27,21,22]	I2	-0.201*	-0.061*	1.088	0	0	1	[27,21,22]
		1965	[22,17,18]	I2	0.068*	0.898	-0.058*	0	1	0	[22,17,18]
		2395	[1,3,3]	L	-10.985	1.929	8.986	-11	2	9	[1,3,3]
		2789	[3,3,4]	L	-5.961	6.014	0.975	-6	6	1	[3,3,4]
	IGSO	279	[0,1,0]	S	-1.974	-5.173	5.848	-2	-5	6	[0,1,0]
		605	[1,1,0]	S	1.925	-6.038	3.085	2	-6	3	[1,1,0]
		883	[2,1,2]	I1	0.173*	5.025	-4.030	0	5	-4	[2,1,2]
		1093	[2,2,2]	I1	-1.939	0.102*	1.967	-2	0	2	[2,2,2]
		1317	[27,21,22]	I2	-0.191*	-0.118*	1.133	0	0	1	[27,21,22]
		1523	[22,17,18]	I2	-0.081*	1.019	-0.151*	0	1	0	[22,17,18]
		1857	[1,3,3]	L	-10.948	1.964	8.960	-11	2	9	[1,3,3]
		2089	[3,3,4]	L	-6.046	6.140	0.965	-6	6	1	[3,3,4]
	MEO	67	[0,1,0]	S	-2.173	-5.106	5.951	-2	-5	6	[0,1,0]
		179	[1,1,0]	S	1.955	-6.086	2.986	2	-6	3	[1,1,0]
		365	[2,1,2]	I1	0.057*	5.020	-4.014	0	5	-4	[2,1,2]
		475	[2,2,2]	I1	-1.791	0.056*	1.988	-2	0	2	[2,2,2]
		1409	[27,21,22]	I2	-0.083*	-0.134*	0.942	0	0	1	[27,21,22]
		1619	[22,17,18]	I2	0.036*	1.013	0.048*	0	1	0	[22,17,18]
		1777	[1,3,3]	L	-10.944	1.860	9.044	-11	2	9	[1,3,3]
		1913	[3,3,4]	L	-6.187	6.136	1.100	-6	6	1	[3,3,4]
case-2	GEO	61	[0,0,1]	S	1.002	-0.952	2.063	1	-1	2	[0,0,1]
		785	[1,1,0]	S	-0.999	1.026	-1.052	-1	1	-1	[1,1,0]
		1407	[1,2,2]	I1	-0.013*	-0.960	4.975	0	-1	5	[1,2,2]
		2087	[1,3,1]	I1	-1.995	0.032*	5.053	-2	0	5	[1,3,1]
		2833	[4,3,3]	I2	0.005*	0.962	0.143*	0	1	0	[4,3,3]
		3509	[2,1,2]	I2	0.998	-0.063*	-0.128*	1	0	0	[2,1,2]
		4275	[3,2,1]	L	-1.007	1.997	-2.933	-1	2	-3	[3,2,1]
		4857	[5,7,6]	L	-0.974	-0.941	10.969	-1	-1	11	[5,7,6]
	IGSO	61	[0,0,1]	S	1.000	-1.034	1.986	1	-1	2	[0,0,1]
		785	[1,1,0]	S	-0.984	1.072	-1.012	-1	1	-1	[1,1,0]
		1407	[1,2,2]	I1	0.014*	-0.964	5.030	0	-1	5	[1,2,2]
		2087	[1,3,1]	I1	-1.990	0.025*	5.062	-2	0	5	[1,3,1]
		2833	[4,3,3]	I2	0.006*	1.007	-0.018*	0	1	0	[4,3,3]
		3509	[2,1,2]	I2	1.003	0.092*	0.048*	1	0	0	[2,1,2]
		4275	[3,2,1]	L	-0.994	2.001	-2.983	-1	2	-3	[3,2,1]
		4857	[5,7,6]	L	-0.978	-0.975	11.055	-1	-1	11	[5,7,6]
	MEO	61	[0,0,1]	S	0.994	-1.009	1.997	1	-1	2	[0,0,1]
		785	[1,1,0]	S	-1.008	0.975	-1.056	-1	1	-1	[1,1,0]
		1407	[1,2,2]	I1	-0.007*	-1.011	4.994	0	-1	5	[1,2,2]
		2087	[1,3,1]	I1	-1.993	-0.023*	4.943	-2	0	5	[1,3,1]
		2833	[4,3,3]	I2	-0.005*	1.012	0.010*	0	1	0	[4,3,3]
		3509	[2,1,2]	I2	1.013	0.010*	0.059*	1	0	0	[2,1,2]
		4275	[3,2,1]	L	-1.005	1.957	-3.033	-1	2	-3	[3,2,1]
		4857	[5,7,6]	L	-0.989	-0.956	11.015	-1	-1	11	[5,7,6]

So (2,1,2) can only be detected by combination [−1, −5,6] and combination [−3,6, −2], while it cannot be detect by combination [4, −2, −3]. In the same way, the cycle slip (27,21,22) can only be detected by combination [−3,6, −2]. But it is enough to indicate that cycle slip occurs, so the cycle slip can also be detected and corrected by the linearly independent combinations.

However, the above analyses cannot exclude contingency, so further work is still needed. Three groups of cycle slips are separately added to the phase data of different orbit types randomly. The first group (G1) that includes (0,0,1), (0,1,0), (1,0,0), (1,1,0), (1,0,1), and (0,1,1) belongs to the small cycle slips. The second group (G2) that includes (2,1,2), (1,1,1), (2,1,0), (27,21,22), (26,20,21), and (22,17,18) belongs to the

TABLE 8. The detection performance of the phase-Doppler combination model (P-D model) and the pseudorange-phase combination model (P-P model) when the cycle slips of the corresponding groups are randomly added to the three types of orbits for case-1 and case-2, respectively.

Case	Orbit Type	Cycle Slip Group	Cycle Slip Type	Total Number of Cycle Slips Added	Corresponding Number of Cycle Slips Detected and Corrected	
					P-D model	P-P model
case-1	GEO	G1	S	1235	1235 (1155/80)	1155
		G2	I	1025	1025 (968/57)	968
		G3	L	1312	1312 (1279/33)	1279
	IGSO	G1	S	775	775 (755/20)	755
		G2	I	738	738 (724/14)	724
		G3	L	758	758 (758/0)	758
	MEO	G1	S	518	518 (509/9)	509
		G2	I	504	504 (499/5)	499
		G3	L	547	547 (542/5)	542
case-2	GEO	G4	S	2685	2685 (2237/448)	2237
		G5	I	2837	2837 (2326/511)	2326
		G6	L	2944	2944 (2460/484)	2460
	IGSO	G4	S	2892	2892 (2531/361)	2531
		G5	I	3317	3317 (3055/262)	3055
		G6	L	2957	2957 (2699/258)	2699
	MEO	G4	S	3165	3165 (2879/286)	2879
		G5	I	2903	2903 (2742/161)	2742
		G6	L	3304	3304 (3074/230)	3074

insensitive cycle slips. The third group (G3) that includes (1,3,3), (3,3,4), (2,7,6), (5,9,8), (12,11,19), and (21,23,17) belongs to the large cycle slips.

To keep all the insensitive cycle slips in G2 unchanged, values of the coefficients $[i,j,k]$ of the pseudorange-phase combination model are identical with the values of the phase-Doppler combination model, and the above principle is also adopted in case-2. In addition, as shown in section III, values of the coefficients l, m, and n of the pseudorange-phase combination model are all equal to 1/3. Table 8 lists the results of cycle slips detection and correction with the phase-Doppler combination model (P-D model) and the pseudorange-phase combination model (P-P model). For the reason that the triple-frequency pseudorange observations at some epochs do not exist, the detection and correction results of the phase-Doppler combination model in the sixth column of Table 8 are divided into three parts. The three parts are in the form of I (II/III):

(1) The part I represents the total number of cycle slips that are detected and corrected successfully.

(2) The part II in the bracket represents the detection and correction results when all the Doppler and pseudorange observations at some epochs exist.

(3) The part III represents the detection and correction results when all the Doppler observations at some epochs exist, and the pseudorange observations at the corresponding epochs are missing.

It can be seen from Table 8 that all the cycle slips added are detected and corrected successfully by the two models. Moreover, when some pseudorange observations at some epochs are missing, the phase-Doppler combination model can also detect and correct all the three types of cycle slips. So it can be concluded that the phase-Doppler combination model is an effective method to detect cycle slips when the ionosphere is steady, and the sampling interval is 30 s.

C. CYCLE SLIPS DETECTION AND CORRECTION WITH CASE-2

Section B has verified the effectiveness of the phase-Doppler model under 30 s sampling interval. According to section III, the phase-Doppler combination model is also affected by sampling intervals. So case-2 with 1 s sampling interval is also needed. Combined with Table 3, the linearly independent combinations [0, −1,1], [1,0, −1], and [−3,2,2] are selected for case-2. Figs. 11-13 show the differencing values ($\Delta\tilde{N}_{(i,j,k)}$) of the cycle slips detection combinations on GEO, IGSO, and MEO for case-2 when no cycle slip occurs, respectively. From the three figures, it can be seen that all the differencing values are smaller than 0.08 cycles, 0.13 cycles, and 0.24 cycles, respectively. So no cycle slip exists.

For case-2, the A-matrix in (28) becomes

$$\mathrm{A} = \begin{bmatrix} 0 & -1 & 1 \\ 1 & 0 & -1 \\ -3 & 2 & 2 \end{bmatrix} \tag{34}$$

So the four different types of cycle slips that are added to the phase data turn into (0,0,1) (S) and (1,1,0) (S), (1,2,2) (I1) and (1,3,1) (I1), (4,3,3) (I2) and (2,1,2) (I2), (3,2,1) (L) and (5,7,6) (L). Figs. 14-16 show the results of the cycle slips detection and correction by the phase-Doppler combination model, and the results are also listed in Table 7. Combined with Figs. 11-13, it can be seen that after the above cycle slips are added, obvious changes occur consistently. All the four types of cycle slips added can be detected and corrected successfully like case-1.

However, the data used in Figs. 11-16 only cover no more than 1.5 hours. Therefore, to reduce the influence of some accidental factors, three groups of cycle slips are separately added to the phase data of the whole day randomly. And the three groups of case-2 are different from those of case-1 for the reason that the detection combinations of them are

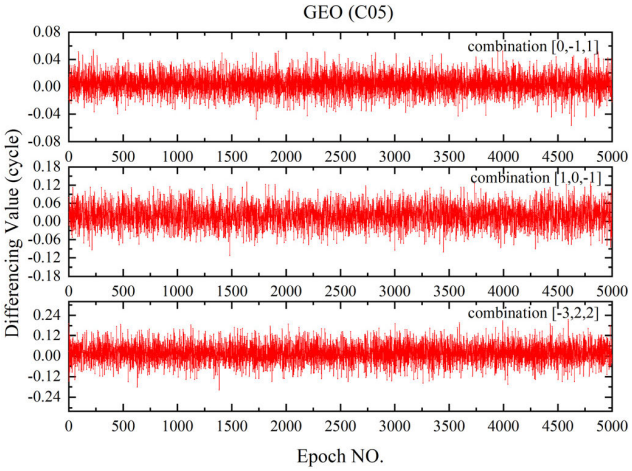

FIGURE 11. Differencing values ($\Delta\tilde{N}_{(i,j,k)}$) of the cycle slips detection combinations on GEO for case-2, when no cycle slip occurs.

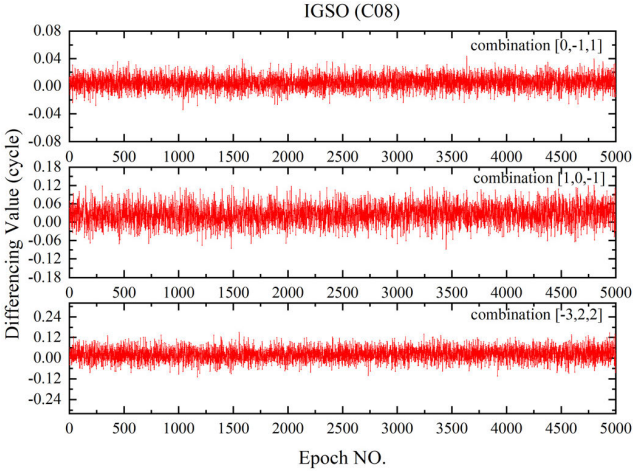

FIGURE 12. Differencing values ($\Delta\tilde{N}_{(i,j,k)}$) of the cycle slips detection combinations on IGSO for case-2, when no cycle slip occurs.

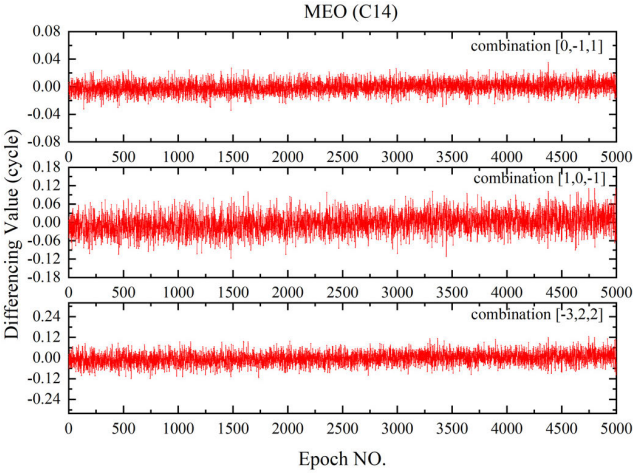

FIGURE 13. Differencing values ($\Delta\tilde{N}_{(i,j,k)}$) of the cycle slips detection combinations on MEO for case-2, when no cycle slip occurs.

different. The first group (G4) that includes (0,0,1) and (1,1,0) belongs to the small cycle slips. The second group (G5) that

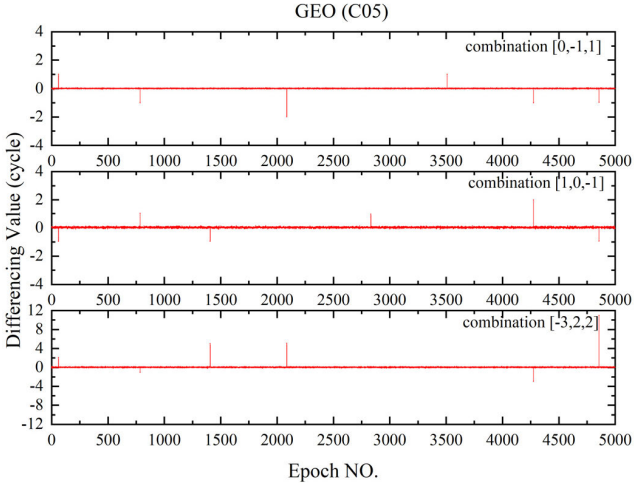

FIGURE 14. Differencing values ($\Delta\tilde{N}_{(i,j,k)}$) of the cycle slips detection combinations of the phase-Doppler combination model on GEO for case-2, when the four types of cycle slips are added.

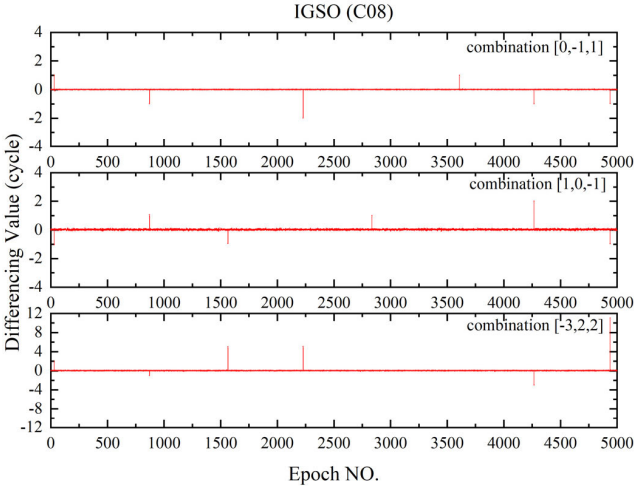

FIGURE 15. Differencing values ($\Delta\tilde{N}_{(i,j,k)}$) of the cycle slips detection combinations of the phase-Doppler combination model on IGSO for case-2, when the four types of cycle slips are added.

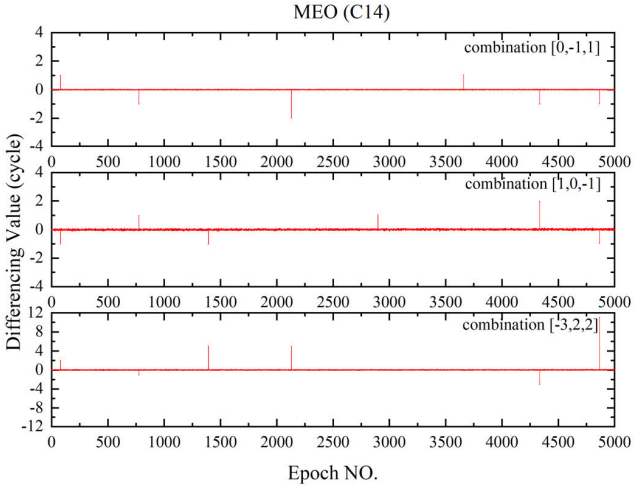

FIGURE 16. Differencing values ($\Delta\tilde{N}_{(i,j,k)}$) of the cycle slips detection combinations of the phase-Doppler combination model on MEO for case-2, when the four types of cycle slips are added.

includes (0,1,1), (0,1,0), (2,2,1), (1,1,1), (4,3,3), and (2,1,2) belongs to the insensitive cycle slips. The third group (G6) that includes (2,7,6), (3,2,1), (3,8,10), (5,7,6), (12,11,19), and (21,23,17) belongs to the large cycle slips.

Table 8 also lists the results of cycle slips detection and correction with the two models. It can also be concluded that the two models can detect and correct all the three groups of cycle slips successfully when the sampling interval is 1 s. And when some pseudorange observations are missing, all the cycle slips can also be detected and corrected successfully by the phase-Doppler combination model.

In conclusion, according to the results of case-1 and case-2 in Table 8, the phase-Doppler combination model achieves the same performance as the pseudorange-phase combination model. In addition, the advantages of methods that combine triple-frequency pseudorange and phase observations over some other existing methods have been presented and explained in section I. So the proposed method in the paper can be a choice for cycle slips detection, especially when the pseudorange observations are missing. And it can detect small, insensitive, and large cycle slips successfully under steady ionosphere with 30 s and 1 s sampling intervals.

V. CONCLUSION

A new cycle slips detection and correction method based on the triple-frequency carrier phase and Doppler observations is introduced in this article for some harsh and special situations when the valid pseudorange data are missing or insufficient accuracy. Moreover, the effectiveness of the phase-Doppler combination model under steady ionosphere is verified when the sampling interval is 30 s and 1 s. And all the cycle slips that are added to the phase measurements of different types of BDS satellites (GEO, IGSO, MEO) can be detected and corrected successfully.

However, there still exist many problems that need to be further resolved. The performance of the phase-Doppler combination model under the kinematic situation, higher ionospheric activity, other sampling intervals, and larger Doppler noise should be further researched. Maybe compensating for ionosphere and Doppler noise will be needed. Whether a more accurate way of fitting in (21) exists is needed to be studied. In general, the new model still needs to be further improved and completed in different situations.

In addition, to reduce the impact of the ionospheric delay, the second-order time-difference phase-Doppler combination method can be further studied as well.

REFERENCES

[1] P. J. G. Teunissen, R. Odolinski, and D. Odijk, "Instantaneous BeiDou+GPS RTK positioning with high cut-off elevation angles," *J. Geodesy*, vol. 88, no. 4, pp. 335–350, 2014.

[2] S. B. Bisnath and R. B. Langley, "Efficient, automated cycle-slip correction of dual-frequency kinematic GPS data," in *Proc. ION GPS*, 2000, pp. 145–154.

[3] X. W. Chang, X. Yang, and T. Zhou, "MLAMBDA: A modified LAMBDA method for integer least-squares estimation," *J. Geodesy*, vol. 79, no. 9, pp. 552–565, Dec. 2005.

[4] J. Chen, D. Yue, S. Zhu, Z. Liu, X. Zhao, and W. Xu, "A new cycle slip detection and repair method for galileo four-frequency observations," *IEEE Access*, vol. 8, pp. 56528–56543, 2020.

[5] G. Beutler and D. Davidson, "Some theoretical and practical aspects of geodetic positioning using carrier phase difference observations of GPS satellites," Univ. New Brunswick, Fredericton, NB, Canada, Tech. Rep. 109, 1984.

[6] B. Hofmann-Wellenhof, H. Lichtenegger, and E. Wasle, *GNSS—Global Navigation Satellite Systems GPS, GLONASS, Galileo, and More*. Vienna, Austria: Springer, 2008, pp. 647–651.

[7] W. Feng, Y. Zhao, L. Zhou, D. Huang, and A. Hassan, "Fast cycle slip determination for high-rate multi-GNSS RTK using modified geometry-free phase combination," *GPS Solutions*, vol. 24, no. 2, p. 42, Apr. 2020.

[8] M. Cocard, S. Bourgon, O. Kamali, and P. Collins, "A systematic investigation of optimal carrier-phase combinations for modernized triple-frequency GPS," *J. Geodesy*, vol. 82, no. 9, pp. 555–564, Sep. 2008.

[9] B. Li, T. Liu, L. Nie, and Y. Qin, "Single-frequency GNSS cycle slip estimation with positional polynomial constraint," *J. Geodesy*, vol. 93, no. 9, pp. 1781–1803, Sep. 2019.

[10] G. Blewitt, "An automatic editing algorithm for GPS data," *Geophys. Res. Lett.*, vol. 17, no. 3, pp. 199–202, Mar. 1990.

[11] R. Hatch, "The synergism of GPS code and carrier measurements," in *Proc. 3rd Int. Symp. Satell. Doppler Positioning*, vol. 2, Feb. 1982, pp. 1213–1232.

[12] W. Melbourne, "The case for ranging in GPS-based geodetic systems," in *Proc. 1st Int. Symp. Precise Positioning Global Positioning Syst.*, Rockville, MD, USA, 1985, pp. 373–386.

[13] G. Wübbena, "Software developments for geodetic positioning with GPS using TI-4100 code and carrier measurements," in *Proc. 1st Int. Symp. Precise Positioning Global Positioning Syst.*, Rockville, MD, USA, vol. 19, 1985, pp. 403–412.

[14] C. Cai, Z. Liu, P. Xia, and W. Dai, "Cycle slip detection and repair for undifferenced GPS observations under high ionospheric activity," *GPS Solutions*, vol. 17, no. 2, pp. 247–260, Apr. 2013.

[15] R. Pu and Y. Xiong, "An improved algorithm based on combination observations for real time cycle slip processing in triple frequency BDS measurements," *Adv. Space Res.*, vol. 63, no. 9, pp. 2796–2808, May 2019.

[16] S. Banville and R. B. Langley, "Mitigating the impact of ionospheric cycle slips in GNSS observations," *J. Geodesy*, vol. 87, no. 2, pp. 179–193, Feb. 2013.

[17] M. C. de Lacy, M. Reguzzoni, and F. Sansò, "Real-time cycle slip detection in triple-frequency GNSS," *GPS Solutions*, vol. 16, no. 3, pp. 353–362, Jul. 2012.

[18] Q. Zhao, B. Sun, Z. Dai, Z. Hu, C. Shi, and J. Liu, "Real-time detection and repair of cycle slips in triple-frequency GNSS measurements," *GPS Solutions*, vol. 19, no. 3, pp. 381–391, Jul. 2015.

[19] G. Xiao, M. Mayer, B. Heck, L. Sui, T. Zeng, and D. Zhao, "Improved time-differenced cycle slip detect and repair for GNSS undifferenced observations," *GPS Solutions*, vol. 22, no. 1, p. 6, Jan. 2018.

[20] X. Zhang and P. Li, "Benefits of the third frequency signal on cycle slip correction," *GPS Solutions*, vol. 20, no. 3, pp. 451–460, Jul. 2016.

[21] L. Huang, Z. Lu, G. Zhai, Y. Ouyang, M. Huang, X. Lu, T. Wu, and K. Li, "A new triple-frequency cycle slip detecting algorithm validated with BDS data," *GPS Solutions*, vol. 20, no. 4, pp. 761–769, Oct. 2016.

[22] D. Zhao, G. W. Roberts, C. M. Hancock, L. Lau, and R. Bai, "A triple-frequency cycle slip detection and correction method based on modified HMW combinations applied on GPS and BDS," *GPS Solutions*, vol. 23, no. 1, p. 22, Jan. 2019.

[23] B. Li, Y. Qin, and T. Liu, "Geometry-based cycle slip and data gap repair for multi-GNSS and multi-frequency observations," *J. Geodesy*, vol. 93, no. 3, pp. 399–417, Mar. 2019.

[24] L. Yin, S. Li, Z. Deng, and D. Zhu, "A novel cycle slips detection model for the high precision positioning," *IEEE Access*, vol. 7, pp. 24041–24050, 2019.

[25] P. Li, X. Jiang, X. Zhang, M. Ge, and H. Schuh, "Kalman-filter-based undifferenced cycle slip estimation in real-time precise point positioning," *GPS Solutions*, vol. 23, no. 4, p. 99, Oct. 2019.

[26] G. Chang, T. Xu, Y. Yao, and Q. Wang, "Adaptive Kalman filter based on variance component estimation for the prediction of ionospheric delay in aiding the cycle slip repair of GNSS triple-frequency signals," *J. Geodesy*, vol. 92, no. 11, pp. 1–13, 2018.

[27] M. E. Cannon, K. P. Schwarz, M. Wei, and D. Delikaraoglou, "A consistency test of airborne GPS using multiple monitor stations," *Bull. Géodésique*, vol. 66, no. 1, pp. 2–11, 1992.

[28] P. Cederholm and D. Plausinaitis, "Cycle slip detection in single frequency GPS carrier observations using expected Doppler shift," *Nordic J. Surveying Real Estate Res.*, vol. 10, no. 1, pp. 63–79, 2014.
[29] Z. Dai, "MATLAB software for GPS cycle-slip processing," *GPS Solutions*, vol. 16, no. 2, pp. 267–272, Apr. 2012.
[30] G. Xu, *GPS: Theory, Algorithms and Applications*, 2nd ed. Berlin, Germany: Springer, 2007, pp. 10–74.
[31] J. Zhao, M. Hernández-Pajares, Z. Li, L. Wang, and H. Yuan, "High-rate Doppler-aided cycle slip detection and repair method for low-cost single-frequency receivers," *GPS Solutions*, vol. 24, no. 3, pp. 1–13, Jul. 2020.
[32] Y. Qin, B. Li, and L. Lou, "Multi-frequency BeiDou cycle slip and data gap repair with geometry-based model," in *Proc. Forum Cooperat. Positioning Service (CPGPS)*, May 2017, pp. 251–257.
[33] Y. Feng, "GNSS three carrier ambiguity resolution using ionosphere-reduced virtual signals," *J. Geodesy*, vol. 82, no. 12, pp. 847–862, Dec. 2008.
[34] P. J. G. Teunissen, "Success probability of integer GPS ambiguity rounding and bootstrapping," *J. Geodesy*, vol. 72, no. 10, pp. 606–612, Oct. 1998.
[35] B. Li, S. Verhagen, and P. J. G. Teunissen, "Robustness of GNSS integer ambiguity resolution in the presence of atmospheric biases," *GPS Solutions*, vol. 18, no. 2, pp. 283–296, Apr. 2014.

ZENGKAI SHI received the B.S. degree from the University of Science and Technology of China, in 2015, and the M.S. degree from Space Engineering University, Beijing, China, in 2018, where he is currently pursuing the Ph.D. degree. His current research interests include PNT, BDS positioning, PPP, cycle slip detection, and correction under harsh environment.

XURONG DONG received the Ph.D. degree in inertial positioning and geodesy from the Wuhan Technical University of Surveying and Mapping. He is currently a Professor with the Department of Satellite Positioning and Navigation, Space Engineering University, Beijing. His research interest includes GPS/INS integrated positioning.

XIANGXIANG FAN received the B.S. degree from the Shandong University of Technology, in 2017, and the M.S. degree from Space Engineering University, in 2019. His research interests include global navigation satellite systems, cycle slip detection, and integrated positioning.

GANG ZHANG received the B.S. degree from Xi'an Polytechnic University, in 2011, and the M.S. degree from Xidian University, in 2014. He is currently pursuing the Ph.D. degree with Space Engineering University, Beijing. His research interests include synthetic aperture radar imaging, image interpretation, targets detection, and deep learning.

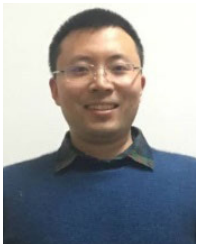

ZHAOYONG QIAN received the B.S. and M.S. degrees from Guizhou University, China. He is currently pursuing the Ph.D. degree with Space Engineering University, Beijing. His research interests include data mining and intelligent algorithm.